The bacteriophage φ29 head–tail connector imaged at high resolution with the atomic force microscope in buffer solution

Daniel J.Müller[1,2], Andreas Engel[1,3], José L.Carrascosa[4] and Marisela Vélez[5]

[1]M.E.Müller-Institute for Microscopic Structural Biology, Biozentrum, University of Basel, Klingelbergstrasse 70, CH-4056 Basel, Switzerland, [2]Forschungszentrum Jülich, IBI-2: Structural Biology, D-52425 Jülich, Germany, [4]Centro Nacional de Biotecnología, CSIC and [5]Laboratorio de Bajas Temperaturas, Departmento Física de la Materia Condensada, C-III, Universidad Autónoma de Madrid, E-28049 Madrid, Spain.

[3]Corresponding author

The surfaces of two- and three-dimensional φ29 connector crystals were imaged in buffer solution by atomic force microscopy (AFM). Both topographies show a rectangular unit cell with dimensions of 16.5 nm × 16.5 nm. High resolution images of connectors from the two-dimensional crystal surface show two connectors per unit cell confirming the p42$_1$2 symmetry. The height of the connector was estimated to be at least 7.6 nm, a value close to that found in previous studies using different techniques. The 12 subunits of the wide connector domain were clearly resolved and showed a right-handed vorticity. The channel running along the connector had a diameter of 3.7 nm in the wide domain, while it was 1.7 nm in the narrow domain end, thus suggesting a tronco-conical channel shape. Moreover, the narrow connector end appears to be rather flexible. When the force applied to the stylus was between 50 and 100 pN, the connector end was fully extended. At forces of ~150 pN, these ends were pushed towards the crystal surface. The complementation of the AFM data with the three-dimensional reconstruction obtained from electron microscopy not only confirmed the model proposed, but also offers new insights that may help to explain the role of the connector in DNA packing.
Keywords: atomic force microscopy/conformational change/φ29 connectors/three-dimensional structure

Introduction

Bacteriophage assembly is a complex process that involves specific interactions to mature unassembled structural components into well-defined intermediates of the viral particle. In this process, the proteins of the head–tail connecting region (connectors or portal proteins) are implicated in the first steps of prohead assembly and in the translocation of DNA inside the viral head. All the different connectors studied so far consist of an outer region with several domains, and an inner tubular region with a channel (reviewed by Valpuesta and Carrascosa, 1994). Connectors from the T4 phage (Driedonks *et al.*, 1981), the T3 phage (Carazo *et al.*, 1986b) and the λ phage

(Kochan *et al.*, 1984) exhibit a 12-fold rotational symmetry. Intact necks extracted from phage φ29 particles which are built from the connector protein (p10) and an additional protein (p11) possess a 12-fold rotational symmetry as well (Carrascosa *et al.*, 1982). However, other connectors, such as those from the SPP1 phage, show 13 morphological subunits (Dube *et al.*, 1993). Connectors of phage T7 (Kocsis *et al.*, 1995; Cerritelli and Studier, 1996) and phage φ29 (Carrascosa *et al.*, 1985; Carazo *et al.*, 1986a; Tsuprun *et al.*, 1994) assembled from overexpressed proteins using cloned genes exhibit polymorphic variants containing 12 and 13 subunits. The significance of this variation is unclear, although, at least for φ29, the physiologically relevant necks (Carrascosa *et al.*, 1982; Carazo *et al.*, 1985) and 9 Å resolution data from frozen–hydrated connector protein crystals (Valpuesta *et al.*, 1994) display a 12-fold symmetry.

The three-dimensional reconstruction from electron microscopy data of the φ29 connector arranged in two-dimensional crystals shows an open channel running along the H axis connectors (Carazo *et al.*, 1986a). In contrast, the channel was found to be closed in necks of connectors extracted from viral particles (Carazo *et al.*, 1985). The presence of two conformational states of the channel suggested an active role for the connector in DNA packaging (Carrascosa *et al.*, 1990). DNA-binding studies carried out with φ29 connectors *in vitro* have demonstrated that there is a clear affinity of the connector for DNA ends (Herranz *et al.*, 1990) and also different binding behavior depending on the DNA structure (Turnquist *et al.*, 1992; Valpuesta *et al.*, 1992; Urbaneja *et al.*, 1994). Furthermore, linear DNA has been proposed to interact with the connector channel (Valle *et al.*, 1996).

Despite these extensive structural and functional analyses, the surface topography of the outer and inner domain of the connector are not well resolved. We have established conditions to reproducibly acquire topographs of membrane proteins at subnanometer resolution using the atomic force microscope (AFM) (Karrasch *et al.*, 1994; Müller *et al.*, 1995b; Schabert *et al.*, 1995). Directly observed conformational changes of single bacteriorhodopsin loops (Müller *et al.*, 1995a) induced by the interaction with the AFM stylus demonstrate the sensitivity of this technique. In addition, the observed time-dependent opening and closing of single pores of an eubacterial surface layer (Müller *et al.*, 1996) underline the potential of the AFM to monitor biological processes. In this work, we demonstrate that the 12 subunits of the outer domain of the φ29 connector can be resolved with the AFM. The new structural information provided by the the AFM is compared with the data from cryo-transmission electron microscopy, and the flexibility of the narrow connector end is discussed.
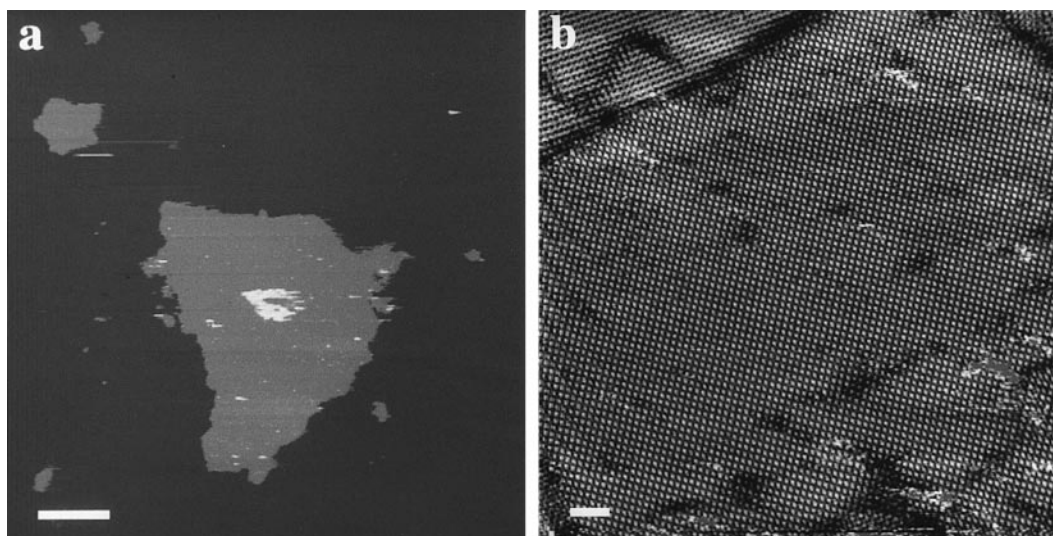
Fig. 1. AFM image of a two-dimensional φ29 connector crystal recorded in buffer solution. (**a**) In the presence of 1 M KCl, the planar sheets adsorbed smoothly onto the freshly cleaved mica surface. The average height of the crystals directly attached to mica was 8.3 ± 0.6 nm. When attached to an underlying crystal sheet the measured height was 8.5 ± 0.5 nm. (**b**) Molecular resolution of the crystal surface. The protrusions representing single connectors were 16.5 nm apart. Imaging conditions: buffer solution (0.5 M KCl, 20 mM Tris–HCl, pH 8.4); applied force ~500 pN; scan frequency 3.8 Hz (original frame size 40 µm) for low resolution and 3.2 Hz for molecular resolution (original frame size 1.4 µm). The scale bars in (a) and (b) are 2.5 µm and 100 nm, respectively. The full gray level range of (a) and (b) is 50 and 4 nm, respectively.

Results

The overexpression of the gene coding for the protein comprising the φ29 connector (p10, M_r = 35 800) in *Escherichia coli* allowed large amounts of connectors to be produced and well-ordered two-dimensional crystals to be assembled (Valpuesta *et al.*, 1994). Imaged in buffer solution with the AFM, these crystals were found to exhibit diameters of >8 µm (Figure 1a). The crystalline sheets adsorbed without fold or cracks onto the freshly cleaved mica surface. This is a prerequisite for high resolution imaging with the AFM (Müller *et al.*, 1995b). The thickness of the sheets adsorbed to mica was 8.3 ± 0.6 nm (*n* = 49). When adsorbed onto a crystalline sheet, the thickness of the upper sheet was 8.5 ± 0.5 nm (*n* = 20). Images recorded at higher magnification showed single connectors assembled into a rectangular lattice (Figure 1b). The unit cell dimensions of 16.5 nm× 16.5 nm ± 0.5 nm were identical to those measured for two-dimensional crystals using electron crystallography (16.5×16.5 nm; Carazo *et al.*, 1986a). Depending on the purification batch used, three-dimensional crystals could be grown (Valpuesta *et al.*, 1994). The low magnification image showed that these three-dimensional crystals were built up from sheet-like structures (Figure 2). At higher magnification (Figure 2, inset), the rectangular arrangement of the connectors was distinct.

Submolecular resolution was achieved only with single layered two-dimensional crystalline sheets (Figure 3). The topography of the connectors strongly depended on the force applied between the stylus and the crystal surface. At the top of the image, the applied force was between 50 and 100 pN (Figure 3; between a and b). The narrow domains of the connectors appeared in their extended conformation. When the force was increased to ~150– 200 pN, the connector ends were compressed and did not protrude from the crystal surface, although the central channel was clearly resolved (Figure 3; between b and c).
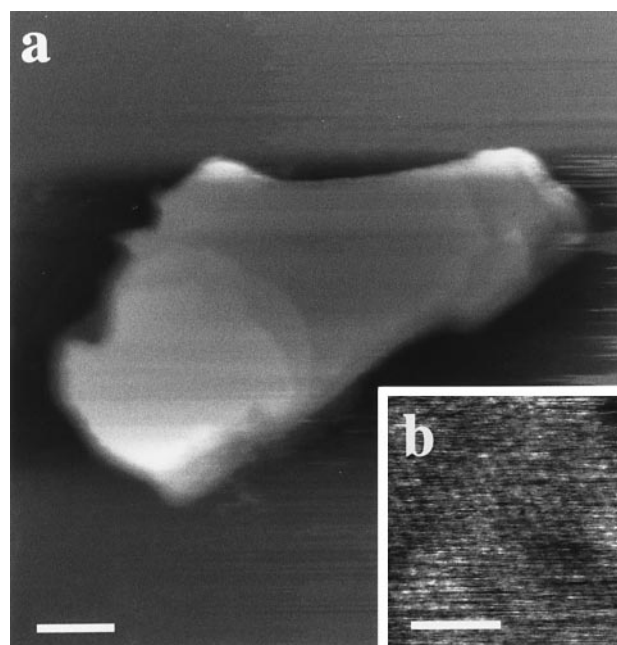

Fig. 2. Three-dimensional crystal of φ29 connectors imaged in buffer solution. (**a**) The layered structure of the crystal was visible. (**b**) Molecular resolution of the connectors located at the crystal surface. Imaging conditions: buffer solution (500 mM KCl, 20 mM Tris–HCl, pH 7.6); applied force ~500 pN; scan frequency 3.6 Hz (original frame size 30 µm) for low resolution and 5.1 Hz for molecular resolution (original frame size 570 nm).The scale bars in (a) and (b) are 5 µm and 50 nm, respectively. The full gray level range of (a) and (b) is 500 and 5 nm, respectively.

When the force was reduced, the extended conformation of φ29 connectors was seen again (Figure 3; between c and d). This structural change was fully reversible and could be repeated several times during continuous scanning and imaging of the same area at high resolution. The narrow connector end was blurred in its extended form
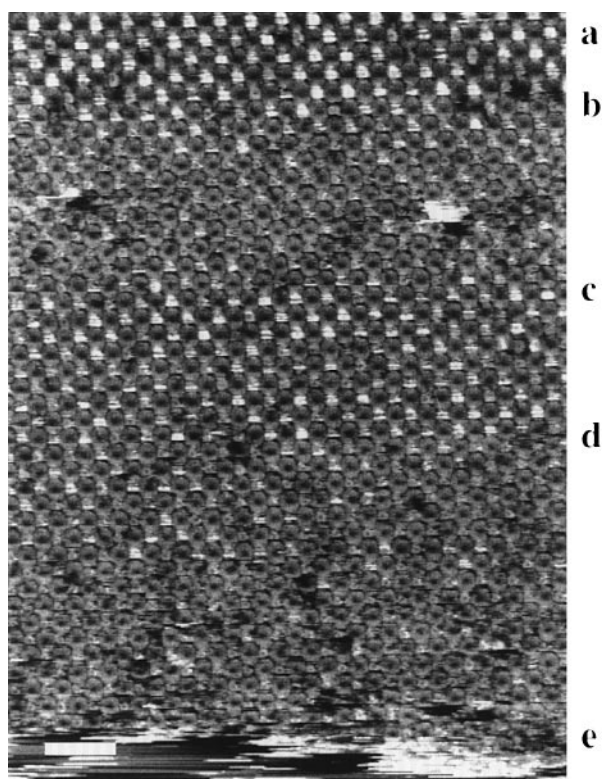
Fig. 3. Force-dependent topography of φ29 connectors acquired with the AFM in buffer solution. Between (a) and (b) the applied force was between 50 and 100 pN. At (b) the force was increased to ~150 pN. The extended protrusions from the narrow connector end were pushed down by the stylus. This reversible process was repeated within the image: the applied force was 50–100 pN between (c) and (d) and 150 pN between (d) and (e). (e) When the force was increased to 300 pN, the crystalline sheet was disrupted by the stylus. Imaging conditions: buffer solution (500 mM KCl, 20 mM Tris–HCl, pH 7.6); scan frequency 3.2 Hz. Scale bar 50 nm, full gray level range 5 nm.

(i.e. when imaged at low force), whereas it was seen as a small rather sharp ring when pushed towards the substrate by the tip. The lower region in Figure 3 (below e) was imaged with a force of ~250–300 pN. At this force, the crystal was disrupted by the interaction with the stylus, and the bare mica surface became visible.

To show the submolecular structures in more detail, the surface of the two-dimensional crystal was imaged at high magnification (Figure 4). At minimum forces (≈50 pN), the narrow end of the connector protruded fully outwards from the surface. While the scanning stylus imaged the holes of the narrow ends of the connectors, it did not interact sufficiently with the wide connector domains to achieve submolecular resolution (Figure 4a). This was not the case in the area of lattice defects (white circle). Here, the subunits of the wide domain of the connector were directly imaged. At large defects, the stylus reached the mica surface, and the height difference from the core of the wide connector end to the mica was determined to be 7.6 ± 0.5 nm. If higher forces were applied to the stylus (Figure 4d), the narrow ends were pushed down towards the surface of the wide connector end. The latter was thus accessible to the tip, and all 12 subunits were often visible in the raw data. As in Figure 3, the narrow connector ends were less sharp in their extended form than when pushed down (compare Figure 4a and d). Occasionally,

only half of these ends were imaged. The 12 subunits of the wide domains were distinct and exhibited a right-handed vorticity in the unprocessed image. In none of the recorded images were 13 subunits observed. To estimate the inner and outer diameter of the narrow connector end, an average of the extended form was calculated from 180 unit cells (Figure 4b), and 4-fold symmetrized (Figure 4c). The unsymmetrized average documents a lateral stretching of the protein in the fast scanning direction. The flexibility was probably responsible for the elliptical distortion and prevented the substructure of the narrow connector domain from becoming distinct in the average. The narrow end protruded by 2.3 ± 0.2 nm ($n = 53$) above the rosette of the wide connector end. The inner diameter was estimated to be 1.7 ± 0.3 nm, and the outer diameter 6.4 ± 0.4 nm, but both the geometry of the AFM tip (Schwarz et al., 1994) and the flexibility of the extended narrow end were likely to influence these values. The measured values of the outer and inner diameters thus represent the maximum and the minimum possible dimensions of the channel, respectively.

Best averaging results of the wide connector domain were achieved after single particle averaging of selected particles (Figure 5). In the average of the wide connector end comprising 183 particles (Figure 5b), the right-handed vorticity that was distinct in unprocessed single particle images (Figure 5a) was enhanced. Each of the 12 subunits was seen not only in the unsymmetrized average (Figure 5b), but could also be discerned in most of the unprocessed views of individual connectors (Figure 5a). The lateral resolution of these topographs was estimated according to the spectral signal-to-noise ratio to 1.8 nm (Unser et al., 1989). The height of the protrusions above the flat inner connector annulus was between 0.15 and 0.40 nm. The rotational power spectrum (Figure 6) of the average displayed in Figure 5b exhibited 2-, 4- and 12-fold components, supporting the 12-fold rotational symmetrization applied to give the final result shown in Figure 5c. The outer diameter of the core was 13.3 ± 0.3 nm, a value that agrees with the projection data obtained by transmission electron microscopy of frozen–hydrated connector crystals at 9 Å resolution (Valpuesta et al., 1994), while the inner diameter was 3.7 ± 0.4 nm. As mentioned above, the geometry of the AFM tip (Schwarz et al., 1994) is likely to influence the measured value of the inner and outer diameter of the connector channel.

The perspective view of the crystal surface was calculated from 4-fold-symmetrized correlation averages of either the extended narrow connector end or the wide connector domain (Figure 7). In agreement with previous results (Carazo et al., 1986a), this view showed two connectors per unit cell oriented in opposite directions and perpendicular to the crystal, consistent with the space group p42$_1$2 described for these crystals by Valpuesta et al. (1994). The 12 protrusions of the wide connector domain were 2.7 ± 0.1 nm apart, and had a height of 0.3 ± 0.1 nm ($n = 81$). The narrow and the wide end of the connector exhibited different channel diameters, suggesting that the shape of the channel is not fully cylindrical, but rather tronco-conical or bottleneck-shaped.
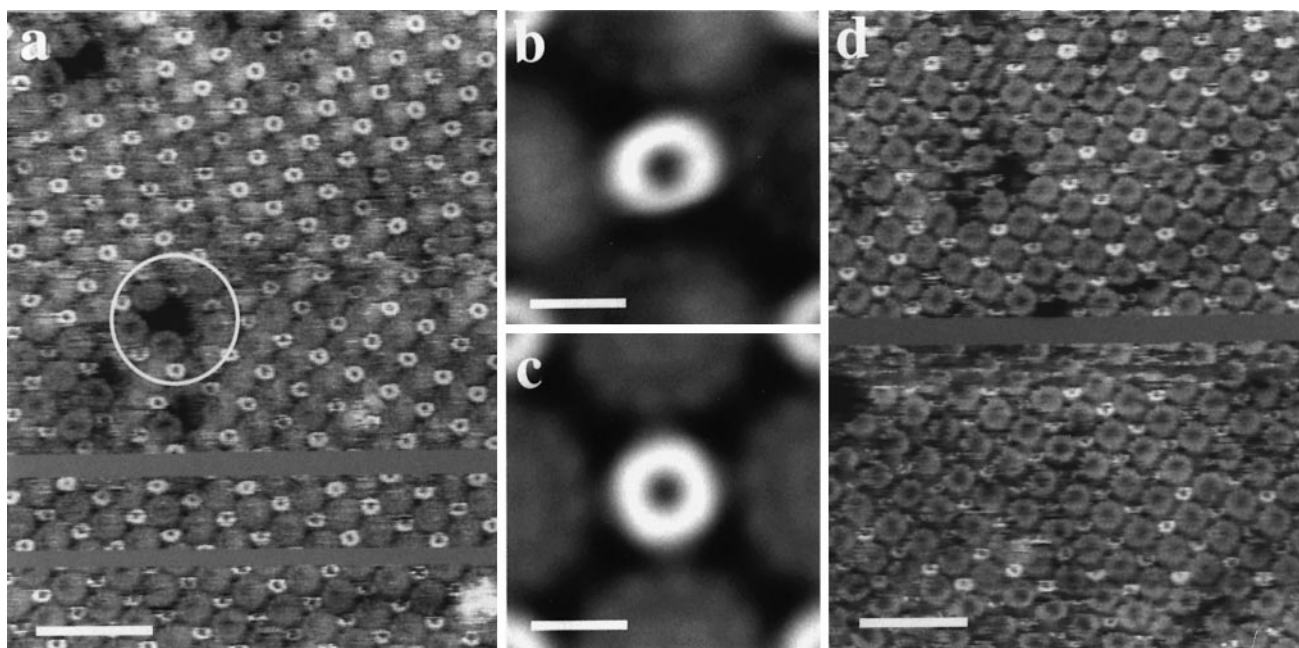
Fig. 4. High resolution topographies of a two-dimensional φ29 connector crystal imaged in buffer solution. (**a**) Connectors imaged at applied forces of 50–100 pN. The narrow connector ends were fully extended. (**b**) The correlation-averaged topography of the narrow end had an elliptical shape with the long axis parallel to the fast scan direction. (**c**) Four-fold-symmetrized correlation average. (**d**) Connectors imaged at 150 pN. Imaging conditions: buffer solution (0.5 M KCl, 20 mM Tris–HCl, pH 8.4); scan frequency 3.8 Hz. The scale bars are 50 nm for (a) and (d), and 5 nm for (b) and (c). The full gray level range is 4 nm for (a) and (d), and 3 nm for (b) and (c).
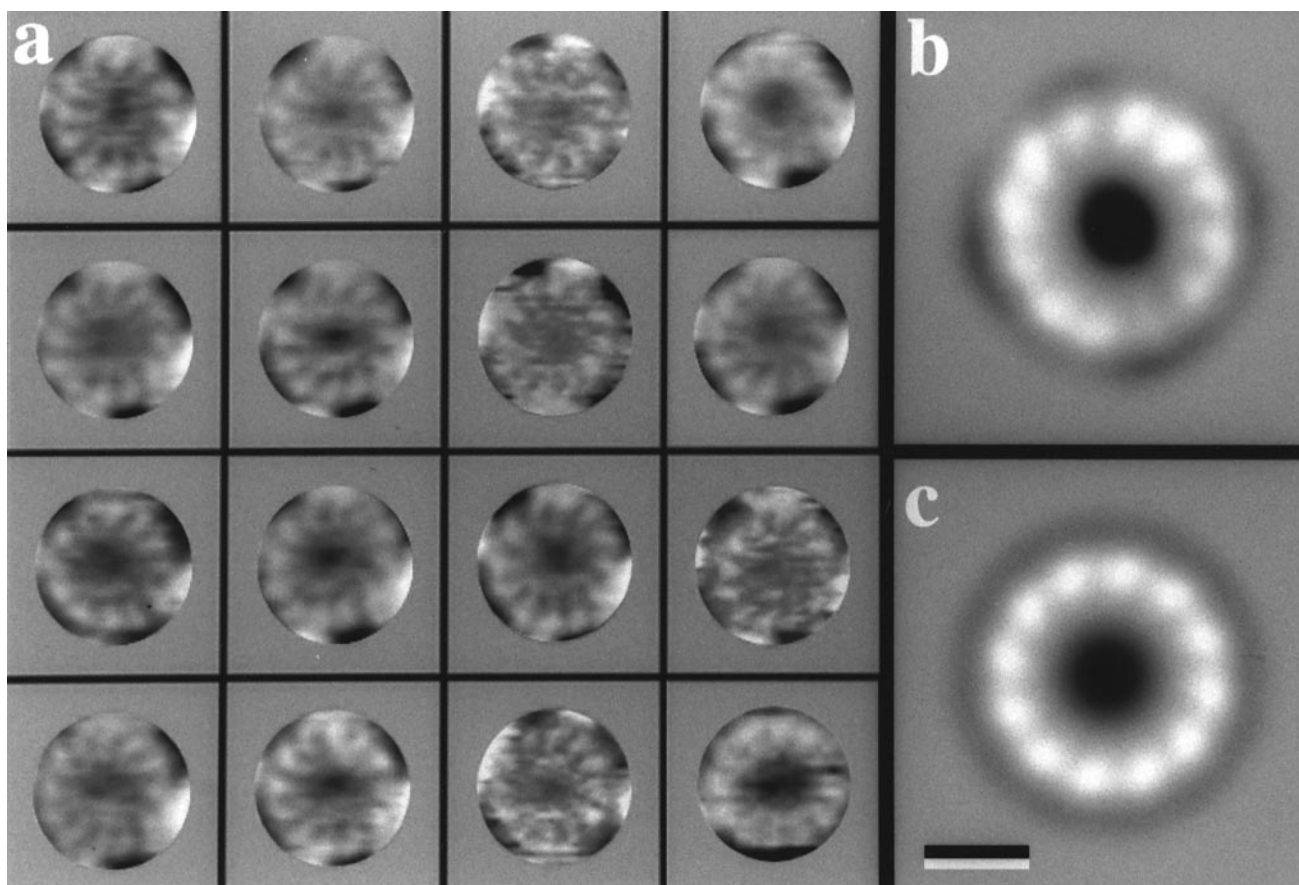

Fig. 5. A gallery of selected particles and their average. (**a**) Wide connector ends recorded with the atomic force microscope in buffer solution. (**b**) Averaged topography from 183 unit cells, generated with the reference-free translational and rotational alignment of the individual particles. (**c**) Twelve-fold rotational symmetrized average based on the spectrum shown in Figure 6. Scale bar 5 nm, full gray level range 3 nm.

Discussion

We recorded topographs with molecular resolution of two- and three-dimensional φ29 connector crystals using the AFM in buffer solution. The tetragonal unit cell exhibited a side length of 16.5 nm and showed two connectors in opposite orientations. Images with submolecular resolution were only obtained from single layered two-dimensional crystal sheets. This indicates that shear forces were sufficient to distort the unstable three-dimensional crystals. High resolution images demonstrate that the narrow end of the connector is rather flexible. At vertical forces of ≥150 pN it was pushed down onto the crystal surface. This either could result from a compression of the narrow end, or the connectors with the narrow end pointing towards the tip could have been pushed down onto the
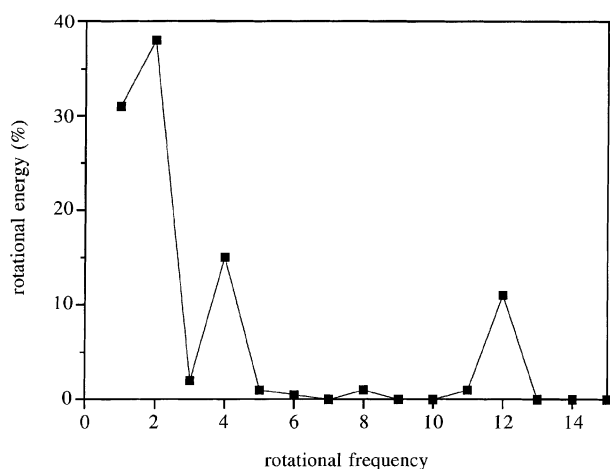

Fig. 6. The rotational power spectrum of the average shown in Figure 5b.

mica. While the latter would explain the rather sharp image of the thin ends at forces of ~150 pN, the force difference of 100–150 pN required to induce the putative compression is remarkably close to the 200 pN reported to produce a conformational change of bacteriorhodopsin (Müller *et al.*, 1995a). However, the binding forces between avidin and biotin (160 pN; Florin *et al.*, 1994), streptavidin and biotin (340 pN; Lee *et al.*, 1994) and between antigen and antibody complexes (60 pN; Dammer *et al.*, 1996) are also within the same range. Therefore, the force does not permit a discrimination between the two postulated mechanisms, a compression (i.e. a conformational change) or a vertical displacement (i.e. a breakage of specific molecular interactions within the crystal). In any case, the deformation of the connectors by ~2.3 nm corresponds to an energy of 55–82 kcal/mol. This low value is compatible with the reversibility of the process. It also implies that the extended narrow connector end was not stable, explaining its stretching along the fast scan direction as well as the low resolution achieved.

The height difference between the surface of the crystalline sheet and the mica surface was 8.3 ± 0.6 nm, while in sheets that formed stacks the height difference was 8.5 ± 0.5 nm. The height of a single connector measured at lattice defects imaged at high magnification (Figure 4a) was 7.6 ± 0.5 nm. Since the narrow connector end protruded 2.3 nm above the wide end, the height of the crystal is calculated to be 9.9 nm, ~1.5 nm more than the heights measured from the low magnification topographs. The pixel size in the latter case, 20 nm, was larger than the unit cell size, 16.5 nm. This implies that an average thickness is measured rather than the total one. Moreover, the force applied by the stylus is different in each case: the force used to measure the crystal thickness was ≥300 pN, whereas forces between 50 and 100 pN were
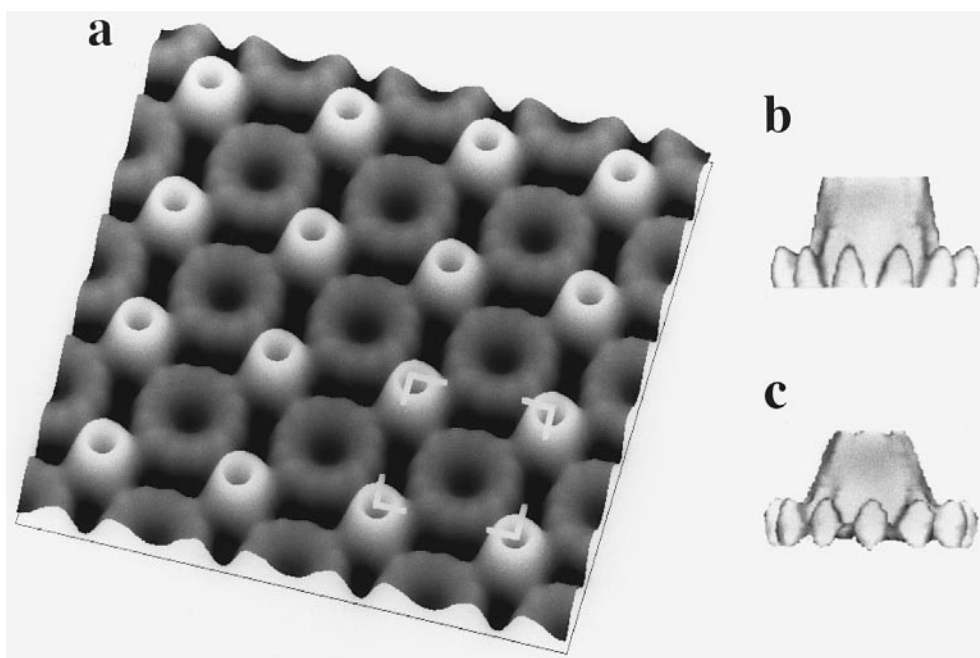

Fig. 7. (**a**) Perspective view of the correlation-averaged and 4-fold-symmetrized topography of the φ29 connector crystal. The topography was obtained from 4-fold-symmetrized correlation averages of both the extended narrow connector end and the wide connector end. The unit cell (indicated by four white corners) has a size of 16.5 nm×16.5 nm. (**b**) Side view from the three-dimensional reconstruction of the connector obtained from tilting series of negatively stained crystals (adapted from Carazo *et al.*, 1986a). (**c**) Side view of the three-dimensional model obtained from the data in (b) after combination with AFM data.

used to obtain high resolution images. It cannot be excluded that the thin connector ends were slightly displaced or deformed even during low force imaging. The measured connector length, 7.6 ± 0.5 nm, is therefore a minimum value. This value agrees with results from other techniques. Three-dimensional reconstruction of a negatively stained specimen (Carazo *et al.*, 1986) gave a height of 7.5 nm, whereas scanning tunneling images of metal replicas of freeze-dried crystals gave a height estimate of 7.0 ± 0.5 nm (Vélez *et al.*, 1996). The thickness of the wide domains of the φ29 connectors can be derived from the height differences recorded with the AFM. Assuming that the narrow ends protrude fully from the crystal surface on both sides, the thickness of the wide domain is calculated to be 2.7 ± 0.6 nm. Thus, the length of the narrow connector end is 5.0 ± 0.8 nm. These values agree within the experimental errors with results from a negatively stained specimen (Carazo *et al.*, 1986a) and from STM measurements (Vélez *et al.*, 1996). However, attachment of biomolecules can result in a flattening of the surface facing the solid support, a phenomenon which is enhanced further by air-drying effects (Kellenberger *et al.*, 1982; Baumeister *et al.*, 1986). Therefore, the results obtained from either negatively stained or freeze-dried samples represent underestimates of the connector dimensions, too.

A distinct structural feature evident in the topographs of the connector crystal recorded with the AFM is the right-handed orientation vorticity of the wide connector end. This feature has been observed less clearly in negatively stained samples (Carazo *et al.*, 1985; Carrascosa *et al.*, 1990), and it may be relevant for understanding the DNA packaging mechanism. In fact, several models proposed before (reviewed in Valpuesta and Carrascosa, 1994) involved some sort of rotational movement for the connector during DNA packaging, either actively coupled to the DNA movement or as a strain-relieving mechanism. In this context, the vorticity of the 12-folded wide connector domain which interacts with the head vortex imposes a defined rotational direction and provides structural support for models relying on an active movement of the connector during DNA translocation (Hendrix, 1978).

Another interesting morphological feature obtained by AFM is the characteristic protrusion of each subunit from the outer surface of the wide domain. This detailed surface information completes the three-dimensional structure of the wide connector end which interacts with the prohead structural proteins. In previous three-dimensional reconstructions from negatively stained samples, this surface information was particularly poor as a result of the limitation imposed by the missing cone inherent to tilt series data (Carazo *et al.*, 1986a) and by alteration of the structure during adsorption (Kellenberger *et al.*, 1982; Baumeister *et al.*, 1986). A comparison of the connector model determined by electron microscopy (Figure 7b) and the model generated with the additional data from AFM topographs illustrates the progress (Figure 7c).

The AFM images have also provided new information showing a difference in the diameter of the channel on the two sides of the connector: while it is 3.7 nm in the wide domain, it is 1.7 nm in the narrow domain. Although these values are likely to be underestimates as a result of tip geometry (Schwarz *et al.*, 1994), it is clear that the shape of the channel is not fully cylindrical, but rather tronco-conical or bottleneck-shaped. The precise definition of the channel structure is important, because the closing of the channel may be linked to the final step of DNA packaging (Carrascosa *et al.*, 1990). A narrow channel end close to the location where the necks extracted from viral particles appear to be plugged (Carazo *et al.*, 1985) supports a model involving small concerted movements of the subunits for the opening/closing mechanism of the channel. As reported for bacteriorhodopsin and the hexagonally packed intermediate layer (HPI), conformational changes can be monitored directly with the AFM (Müller *et al.*, 1995a, 1996). Therefore, predicted conformational changes of the narrow domains (Valpuesta and Carrascosa, 1994) may be observed *in situ* with the AFM. Studies to monitor this process are now in progress.

Materials and methods

Sample preparation

φ29 connectors were obtained from *E.coli* carrying a recombinant plasmid containing the gene encoding protein p10 (M_r = 35 800). The overexpressed p10 was purified by two-step ion exchange chromatography (Ibañez *et al.*, 1984). Large two-dimensional crystals were obtained after incubating a solution of the purified connectors (3–4 mg/ml) at 4°C and increasing the ionic strength of the solution to 2 M NaCl over a few weeks. The crystal-containing stock solution (~10 mg/ml in 2 M NaCl) was diluted 300-fold in 1 M KCl and 20 mM HEPES at pH 7.2. A 25 μl drop of this solution was deposited on freshly cleaved muscovite mica discs (10 mm in diameter) that had been glued onto 25 mm Teflon discs. After 15 min, the sample was rinsed gently with the imaging buffer (0.5 M KCl, 20 mM Tris–HCl, pH 8.4 for two-dimensional crystals) to remove sheets that were not firmly attached.

Atomic force microscopy

After the crystals were adsorbed to mica, the sample was mounted on the piezo scanner of the atomic force microscope (Nanoscope III, Digital Instruments, Santa Barbara, 93117, USA) which was equipped with a liquid cell. Cantilevers purchased from Digital Instruments were 200 μm long and had oxide-sharpened Si_3N_4 tips. The force constant of the cantilevers used to calibrate the applied force was calculated to be 0.15 N/m according to Butt *et al.* (1993) from the cantilever dimensions measured with a scanning electron microscope. After thermal relaxation, the drift of the cantilever deflection angle was at a minimum. Initial engagement of the tip was then performed by setting the scan size to zero to minimize specimen deformation or tip contamination. Prior to scanning the sample, the operating point of the servo system was set to forces below 0.5 nN.

At low magnification (frame size ~600 nm), images were recorded in the error signal mode, acquiring the deflection and height signals simultaneously. The deflection signal was minimized by optimizing gains and scan speed. At high magnification, the deformation of the sample (Weisenhorn *et al.*, 1993) was monitored and minimized by comparing the height profiles acquired in the trace and retrace direction, and at different scan angles. The applied force was corrected manually to compensate for the thermal drift of the microscope.

The 'J'-piezoscanner used had a scan range of 120 μm. Calibration of the scanners was carried out using layered crystals such as mica (Bailey, 1984) and transition metal dichalcogenides (Wilson and Yoffe, 1969) as substrate references. The lateral calibration was carried out by comparing the lattice constants of the layered surface and, for calibration in the *z*-direction, defects (large holes or steps) were used (Jungblut *et al.*, 1992).

Image processing

Image processing was carried out with the SEMPER image processing system (Saxton *et al.*, 1979). Images (512×512 pixels) were flattened line by line prior to calculating correlation averages using a reference unit cell selected from the raw data. Single particle averages were obtained as described (Schabert *et al.*, 1994). Angular harmonics were determined by interpolation of the wide connector end topography to radial coordinates, and integration of the radial interval containing the

most prominent corrugation. The rotational origin has been taken as the center of the channel of the averaged topography. The three-dimensional view of the averaged surface profile (Figure 7) was calculated with the Imagic software (version 0.9d65.0, share ware). Averages from single views of the wide domain were obtained using a variant of the reference-free algorithm described by Penczek *et al.* (1992), using a pyramidal system for particle pre-alignment. The resolution of averages was calculated using the spectral signal-to-noise ratio method (Unser *et al.*, 1989), and the final averages were filtered to that resolution (in this case, 1.8 nm).

Acknowledgements

References

Bailey,S.W. (1984) Micas. *Rev. Mineral.*, **13**.

Baumeister,W., Barth,M., Hegerl,R., Guckenberger,R., Hahn,M. and Saxton,W.O. (1986) Three-dimensional structure of the regular surface layer (HPI layer) of *Deinococcus radiodurans*. *J. Mol. Biol.*, **187**, 241–253.

Butt,H.-J., Siedle,P., Seifert,K., Fendler,K., Seeger,T., Bamberg,E., Weisenhorn,A.L., Goldie,K. and Engel,A. (1993) Scan speed limit in atomic force microscopy. *J. Microsc.*, **169**, 75–84.

Carazo,J.M., Santisteban,A. and Carrascosa,J.L. (1985) Three-dimensional reconstruction of the bacteriophage φ29 neck particles at 2.2 nm resolution. *J. Mol. Biol.*, **183**, 79–88.

Carazo,J.M., Donate,L.E., Herranz,L., Secilla,J.P. and Carrascosa,J.L. (1986a) Three-dimensional reconstruction of the connector of bacteriophage φ29 at 1.8 nm resolution. *J. Mol. Biol.*, **192**, 853–867.

Carazo,J.M., Fujisawa,H., Nakasu,S. and Carrascosa,J.L. (1986b) Bacteriophage T3 gene 8 product oligomer structure. *J. Ultrastruct. Mol. Struct. Res.*, **94**, 105–113.

Carrascosa,J.L., Vinuela,E., Garcia,N. and Santisteban,A. (1982) Structure of the head–tail connector of bacteriophage φ29. *J. Mol. Biol.*, **154**, 311–324.

Carrascosa,J. L., Carazo,J.M., Ibañez,C. and Santisteban,A. (1985) Structure of phage φ29 connector protein assembled *in vivo*. *Virology*, **141**, 190–200.

Carrascosa,J.L., Carazo,J.M., Herranz,L., Donate,L.E. and Secilla,J.P. (1990) Study of two related configurations of the neck of bacteriophage φ29. *Computers Math. Appl.*, **20**, 57–65.

Cerritelli,M.E. and Studier,W. (1996) Purification and characterization of T7 head–tail connectors expressed from the cloned gene. *J. Mol. Biol.*, **258**, 299–307.

Dammer,U., Hegner,M., Anselmetti,D., Wagner,P., Dreier,M., Huber,W. and Güntherodt,H.J. (1996) Specific antigen/antibody interactions measured by force microscopy. *Biophys. J.*, **70**, 2437–2441.

Driedonks,R.A., Engel,A., tenHeggeler,B. and van Driel,R. (1981) Gene 20 product of bacteriophage T4 its purification and structure. *J. Mol. Biol.*, **152**, 641–662.

Dube,P., Tavares,P., Lurz,R. and van Heel,M. (1993) The portal protein of bacteriophage SPP1: a DNA pump with 13-fold symmetry. *EMBO J.*, **12**, 1303–1309.

Florin,E.-L., Moy,V.T. and Gaub,H.E. (1994) Adhesion forces between individual ligand–receptor pairs. *Science*, **264**, 415–417.

Hendrix,R. (1978) Symmetry mismatch and DNA packaging in large DNA bacteriophages. *Proc. Natl Acad. Sci. USA*, **75**, 415–417.

Herranz,L., Bordas,J., Towns-Andrews,E., Mendez,E., Usobiaga,P. and Carrascosa,J.L. (1990) Conformational changes in bacteriophage φ29 connector prevents DNA-binding activity. *J. Mol. Biol.*, **213**, 263–273.

Ibañez,C., García,J.A., Carrascosa,J.L. and Salas,M. (1984) Over-production and purification of the connector protein of *Bacillus subtilis*. *Nucleic Acids Res.*, **12**, 2351–2365.

Jungblut,H., Campbell,S.A., Giersig,M., Müller,D.J. and Lewerenz, H.-J. (1992) Scanning tunneling microscopy observations of biomolecules on layered materials. *Faraday Discuss.*, **94**, 183–198.

Karrasch,S., Hegerl,R., Hoh,J., Baumeister,W. and Engel,A. (1994) Atomic force microscopy produces faithful high-resolution images of protein surfaces in an aqueous environment. *Proc. Natl Acad. Sci. USA*, **91**, 836–838.

Kellenberger,E., Häner,M. and Wurtz,M. (1982) The wrapping phenomenon in airdried and negatively stained preparations. *Ultramicroscopy*, **9**, 139–150.

Kochan,J., Carrascosa,J.L. and Murialdo,H. (1984) Bacteriophage lambda preconnectors. Purification and structure. *J. Mol. Biol.*, **174**, 433–447.

Kocsis,E., Cerritelli,M., Trus,B., Cheng,N. and Steven,A.C. (1995) Improved methods for determination of rotational symmetries in macromolecules. *Ultramicroscopy*, **60**, 219–228.

Lee,G.U., Kidwell,D.A. and Colton,R.J. (1994) Sensing discrete streptavidin–biotin interactions with atomic force microscopy. *Langmuir*, **10**, 354–357.

Müller,D.J., Büldt,G. and Engel,A. (1995a) Force-induced conformational change of bacteriorhodopsin. *J. Mol. Biol.*, **249**, 239–243.

Müller,D.J., Schabert,F.A., Büldt,G. and Engel,A. (1995b) Imaging purple membranes in aqueous solutions at subnanometer resolution by atomic force microscopy. *Biophys. J.*, **68**, 1681–1686.

Müller,D.J., Baumeister,W. and Engel,A. (1996) Conformational change of the hexagonally packed intermediate layer of *Deinococcus radioduruns* imaged by atomic force microscopy. *J. Bacteriol.*, **178**, 3025–3030.

Penczek,P., Radermacher,M. and Frank,J. (1992) Three-dimensional reconstruction of single particles embedded in ice. *Ultramicroscopy*, **40**, 33–53.

Saxton,W.O., Pitt,T.J. and Horner,M. (1979) Digital image processing: the semper system. *Ultramicroscopy*, **4**, 343–354.

Schabert,F. and Engel,A. (1994) Reproducible acquisition of *Escherichia coli* porin surface topographs by atomic force microscopy. *Biophysical J.*, **67**, 2394–2403.

Schabert,F.A., Henn,C. and Engel,A. (1995) Native *Escherichia coli* OmpF porin surfaces probed by atomic force microscopy. *Science*, **268**, 92–94.

Schwarz,U.D., Haefke,H., Reimann,P. and Güntherodt,H.J. (1994) Tip artefacts in scanning force microscopy. *J. Microsc. (Oxford)*, **173**, 183–197.

Tsuprun,V., Anderson,D. and Egelman,E.H. (1994) The bacteriophage φ29 head–tail connector shows 13-fold symmetry in both hexagonally packed arrays and as single particles. *Biophys. J.*, **66**, 2139–2150.

Turnquist,V., Simon,M., Egelman,E.H. and Anderson,D. (1992) Supercoiled DNA wraps around the bacteriophage φ29 head–tail connector. *Proc. Natl Acad. Sci. USA*, **89**, 10479–10483.

Unser,M., Trus,B.L, Frank,J., Steven,A.C. (1989) The spectral signal-to-noise ratio resolution criterion: computational efficiency and statistical precision. *Ultramicroscopy*, **30**, 429–434.

Urbaneja,M.A., Rivas,S., Carrascosa,J.L. and Valpuesta,J.M. (1994) An intrinsic tryptophan fluorescence study of phage φ29 connector/nucleic acid interaction. *Eur. J. Biochem.*, **225**, 747–753.

Valle,M., Valpuesta,J.M., Carrascosa,J.L., Tamayo,J. and Garcia,R. (1996) The interaction of DNA with bacteriophage φ29 connector: a study by AFM and TEM. *J. Struct. Biol.*, **116**, 390–398.

Valpuesta,J.M. and Carrascosa,J.L. (1994) Structure of viral connectors and their function in bacteriophage assembly and DNA packaging. *Q. Rev. Biophys.*, **27**, 107–155.

Valpuesta,J.M., Serrano,M., Donate,L.E., Herranz,L. and Carrascosa,J.L. (1992) DNA conformational change induced by the bacteriophage φ29 connector. *Nucleic Acids Res.*, **20**, 5549–5554.

Valpuesta,J.M., Carrascosa,J.L. and Henderson,R. (1994) Analysis of electron microscope images and electron diffraction patterns of thin crystals of φ29 connectors in ice. *J. Mol. Biol.*, **240**, 281–287.

Vélez,M., Rubio,G., Valpuesta,J.M., Carrascosa,J.L. and Vieira,S. (1996) Topographical images of bacteriophage φ29 connector bidimensional crystals using STM. *Micron*, **27**, 375–380.

Weisenhorn,A.L., Khorsandi,M., Kasas,S., Gotzos,V. and Butt,H.-J. (1993) Deformation and height anomaly of soft surfaces studied with an AFM. *Nanotechnology*, **4**, 106–113.

Wilson,J.A. and Yoffe,A.D. (1969) The transition metal dichalcogenides: discussion and interpretation of the observed optical, electrical and structural properties. *Adv. Phys.*, **18**, 193–335.